The Journal of Pathology: Clinical Research
J Pathol Clin Res July 2025; **11**: e70033
Published online in Wiley Online Library
(wileyonlinelibrary.com). DOI: 10.1002/2056-4538.70033

ORIGINAL ARTICLE

Leveraging deep learning to discover interpretable cellular spatial biomarkers for prognostic predictions based on hepatocellular carcinoma histology

Huijuan Hu[1†], Tianhua Tan[2,3†], Yerong Liu[1], Wei Liang[4], Wei Zhang[5], Jinsong Zhang[5], Ju Cui[6*], Jinghai Song[2,3*] and Xuefei Li[1*]

[1]*State Key Laboratory of Quantitative Synthetic Biology, Shenzhen Institute of Synthetic Biology, Shenzhen Institutes of Advanced Technology, Chinese Academy of Sciences, Shenzhen, PR China*
[2]*Department of General Surgery, Department of Hepatopancreatic Surgery, Beijing Hospital, National Center of Gerontology, Institute of Geriatric Medicine, Chinese Academy of Medical Sciences, Beijing, PR China*
[3]*Graduate School of Peking Union Medical College, Chinese Academy of Medical Sciences, Beijing, PR China*
[4]*School of Mathematical Sciences, Xiamen University, Xiamen, PR China*
[5]*Department of Pathology, Beijing Hospital, National Center of Gerontology, Institute of Geriatric Medicine, Chinese Academy of Medical Sciences, Beijing, PR China*
[6]*The Key Laboratory of Geriatrics, Beijing Institute of Geriatrics, Institute of Geriatric Medicine, Chinese Academy of Medical Science, Beijing Hospital/National Center of Gerontology of National Health Commission, Beijing, PR China*

**Correspondence to: Ju Cui, The Key Laboratory of Geriatrics, Beijing Institute of Geriatrics, Institute of Geriatric Medicine, Chinese Academy of Medical Science, Beijing Hospital/National Center of Gerontology of National Health Commission, Beijing, PR China. E-mail: cuiju4366@bjhmoh.cn; Jinghai Song, Department of General Surgery, Department of Hepatopancreatic Surgery, Beijing Hospital, National Center of Gerontology, Institute of Geriatric Medicine, Chinese Academy of Medical Sciences, Beijing, PR China. E-mail: jhaisong2003@126.com; Xuefei Li, State Key Laboratory of Quantitative Synthetic Biology, Shenzhen Institute of Synthetic Biology, Shenzhen Institutes of Advanced Technology, Chinese Academy of Sciences, Shenzhen, Guangdong, PR China. E-mail: xuefei.li@siat.ac.cn*

[†]*These authors contributed equally to this work.*

Abstract

The spatial structure of various cell types in the tumour microenvironment (TME) can provide valuable insights into disease progression. However, identifying the spatial organization of diverse cell types that significantly correlates with patient prognosis remains challenging. In this study, enabled by deep learning–based cell segmentation and recognition, we developed a computational pipeline to systematically quantify the spatial distribution features of tumour cells, stromal cells, and lymphocytes in haematoxylin and eosin (H&E)–stained pathological images of hepatocellular carcinoma (HCC). We identified six cellular spatial features that consistently and significantly correlated with the overall survival of patients in two independent HCC patient cohorts, The Cancer Genome Atlas Program cohort and the Beijing Hospital cohort. Each threshold for patient stratification was the same for both cohorts, and the six features independently served as prognostic indicators when individually analysed alongside clinical variables. Furthermore, the combination of features such as the mean value of cellular diversity around stromal cells (StrDiv-M), the median distance between all cells (CellDis-MED), and the median value of variation coefficient of the distance around stromal cells and their neighbours (CvStrDis-MED) could further stratify the patient prognosis. In addition, incorporating cell spatial features with another clinical feature, microvascular invasion improved prognostic stratification efficacy for patients from both cohorts. In conclusion, by quantifying the cellular spatial organization features in the HCC TME, we discovered novel biomarkers for evaluating tumour prognosis. These findings could promote mechanistic studies of the cellular spatial organization within the HCC TME and potentially guide future clinical treatment.

Keywords: cell segmentation; cell classification; Delaunay network; cellular diversity; coefficient of variation

Received 6 September 2024; Revised 13 April 2025; Accepted 11 May 2025

No conflicts of interest were declared.

Introduction

Hepatocellular carcinoma (HCC) is the most prevalent form of primary liver cancer [1]. However, the significant heterogeneity of HCC presents challenges for accurate diagnosis and prognostic stratification [2]. Despite the complexity, there exist several well-accepted metrics that have been utilized for HCC prognostic evaluation, such as tumour size and number [3], serological level of alpha-fetoprotein [4,5], and histological features such as the presence or absence of vascular invasion [6]. To further improve the accuracy of patient stratification, in recent years, artificial intelligence-based methods have been developed [7,8], utilizing clinical data and/or the non-invasive imaging data such as computed tomography (CT) [9,10], magnetic resonance [11], and ultrasound [12].

In addition to the non-invasive imaging data, histopathological images have also been used for HCC prognosis evaluation [13–15]. However, most of these studies focused on using image patches instead of individual cells. On the other hand, it has been demonstrated that the locations of specific cell types, such as cancer-associated fibroblasts (CAFs), and the corresponding cellular communications (CAFs-tumour) can play a pivotal role in the HCC patient response to anti-programmed cell death protein 1 (PD1) treatment [16]. In addition, previous studies have also shown that close proximity between tumour and $CD8^+$ T cells, or tumour-infiltrating T cells and B cells could be strong prognostic indicators for HCC [17,18].

To facilitate the discovery of cellular spatial features using standard haematoxylin and eosin (H&E) stained images, a deep learning-based approach has been developed to simultaneously recognize and segment tumour cells, lymphocytes, and other non-malignant cells in pathological images of HCC [19]. This study focused on the imaging characteristics of tumour nuclei and the spatial relationships between tumour cells and lymphocytes [18]. However, the spatial interactions between tumour cells and other non-malignant cells remain unexplored. More importantly, the systematic extraction of cellular spatial features from the complex tumour microenvironment (TME) is challenging. There is growing interest in quantitatively characterizing these features in the TME and identifying their clinical relevance in cancer research [20–23].

This study aims to quantitatively and systematically characterize the TME based on cell locations by simultaneously extracting spatial information of multiple cell types from standard H&E pathological images of patients with HCC.

Materials and methods

Patient information

There are two cohorts of patients with HCC in this study. The first cohort involved 264 patients from The Cancer Genome Atlas (TCGA) Program under the liver hepatocellular carcinoma (LIHC) category; the patient IDs are listed in supplementary material, Table S1. The second cohort involved 67 patients with HCC with available whole-tumour pathological slide images, where all patients received curative hepatectomy between 2012 and 2020 at Beijing Hospital and had no evidence of distant metastasis or previous anticancer treatments prior to surgery. The study was performed according to the declaration of Helsinki and was approved by the ethics review board of Beijing Hospital (2023BJYYEC-432-0). All necessary written informed consent was obtained from patients in the Beijing Hospital cohort. All images were FFPE slides and digitally captured at 40× magnification. For clinical variables, the pathological stage was also mapped into three groups: early (stage I, Ia, Ib), locally advanced (stage II, IIa, IIb), and advanced (stage IIIa, IIIb, IV). Detailed patient information of the two cohorts can be found *via* the following link: https://github.com/huhj/Topological-features.

Histopathological image-processing pipeline

The ImageScope annotation tool was used to manually label the boundaries of regions of interest (ROIs). ROIs were defined by the major malignant region in each pathological image. Within ROIs of each WSI, 20 patches, whose dimensions were 5,000 × 5,000 pixels under 40× magnification (0.25 μm per pixel), were randomly sampled.

To reduce the noise of images, a deconvolution method was adopted [24] to convert the RGB colours of H&E colour space, with the deconvolution matrix [0.6500, 0.7040, 0.2860; 0.2681, 0.5703, 0.7764; 0.7110, 0.4232, 0.5616], where signals from the cell nucleus would be enriched in the haematoxylin channel. Then, to reduce the fragments of the cell nucleus caused by noise, morphological operations consisting of opening and closing [25] were used to process the image of the haematoxylin channel. Subsequently, a level set segmentation technique [26] was applied to detect nuclei locations. The parameters of the segmentation algorithm were typically set as follows: Gaussian smoothing kernel: $\sigma = 1.5$; region term weight: $\lambda = 0.6$; compactness factor: $m = 10$; smoothness term weight: $\alpha = 0.3$; and maximum iterations: $T_{\max} = 50$. Finally, image patches with the size 80×80 pixels centred on the

detected nuclei centroid were extracted from the original selected pathological RGB image (illustrated in Figure 1). Such an image-processing procedure can provide a solid foundation for cell recognition by the deep-learning procedure.

Transfer learning convolutional neural network model

To recognise lymphocytes, tumour cells, and stromal cells effectively and simultaneously in H&E images from patients with HCC, we implemented a transfer learning convolutional neural network (CNN) model, which was developed to recognize cells in lung cancer [27]. All networks received an input image patch sized 80 × 80 pixels, which was normalized to the range [−0.5, 0.5] with R, G, and B channels. As in the original CNN model, an eight-layer deep convolutional neural network was applied, which consists of three convolution layers, three pooling layers, one fully connected layer, and an output layer, as shown in Figure 1. The pooling layer used maximum pooling, and the output layer was a softmax layer with three categories: tumour cell, stromal cell, and lymphocyte. For each image patch, the probability for each of the three categories was predicted, and the highest probability was considered as the predicted class. During training, we initialized the model with pre-trained weights [27] in the lung adenocarcinoma datasets and then fine-tuned the parameters for the softmax layer based on 500 patches of our marked examples in HCC datasets using transfer learning [25].

Construction of the topological features based on tumour cells, stromal cells, and lymphocytes

When the centroid of each cell nucleus was obtained, the Delaunay triangulation algorithm [28] was adopted to construct the spatial topological network, in which each nucleus and its adjacent nuclei were connected by edges. Meanwhile, we also applied a Voronoi diagram [29] which divides the space into many areas based on the closest attributes of the objects. In such a diagram, the distance from any point within a convex polygon's enclosed region to the object point of that polygon is less than the distance to any other object point.

Based on the location of the graph nodes in the graph measurements (i.e., cell positions), we further constructed spatial features that capture the spatial

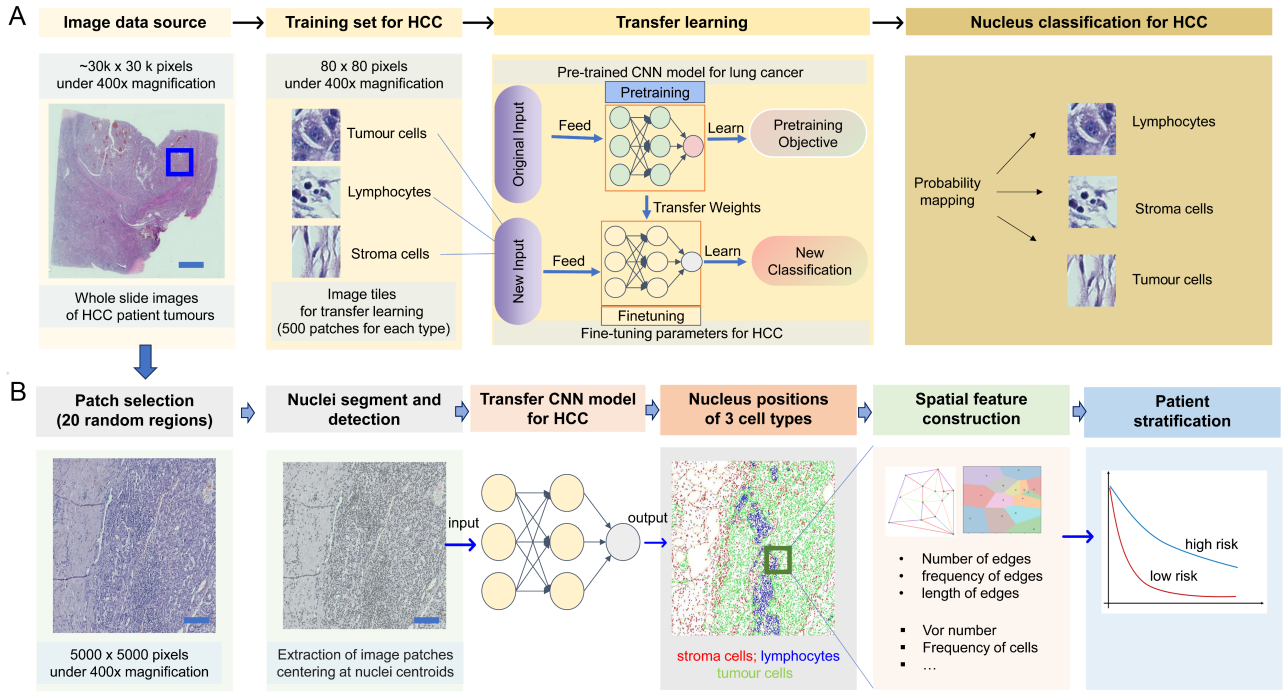

Figure 1. Data acquisition and workflow for the prognostic analysis using H&E pathological images. (A) The cell classification workflow. The nuclei of tumour cells, stromal cells, and lymphocytes are identified through image processing, transfer learning, and classification (see Materials and Methods). (B) The workflow of spatial feature construction and prognosis analysis. We randomly selected 20 ROIs to segment and detect nuclei, and then classified each nucleus using the HCC-CNN model. Delaunay triangulation and Voronoi tessellation were applied to construct 109 quantitative spatial features. Then the prognostic value of proposed features was evaluated.

arrangement and structural characteristics of the TME. In total, we constructed 109 spatial features. A full list of these spatial features is presented in supplementary material, Table S1 with detailed descriptions of their biological meanings. Note that since we selected 20 patches from the whole-slide image (WSI) of each patient, the topological characteristics of the cells for each patient were calculated based on the corresponding values in all patches from the same WSI.

Survival analysis

Once the 109 spatial features were calculated, we first separated each patient cohort into two groups with a specific cut-off value of a particular feature. Next, Kaplan–Meier survival analysis and log-rank tests were performed to test for a significant difference in the overall survival (OS) between the two groups. OS data were obtained from TCGA and Beijing Hospital, documented in https://github.com/huhj/Topological-features and censored to the right. Specifically, for each feature, we selected the optimal cut-off value to divide the patients into two groups using the R package survminer, which uses the maximum selected rank statistic to test for independence between the response variable and the given feature. In addition, a univariate and multivariate Cox proportional hazard model was used to estimate the hazard ratios (HRs) and the 95% confidence intervals (CI). A two-sided p value of 0.05 was selected as the threshold to define statistical significance between patient groups. The survival risk ratio (HR) was used to represent the difference in risk between different groups due to the variable intervention. All variables with log-rank $p < 0.05$ on univariate analysis were entered into the multivariate analysis with backward stepwise selection of variables. R (version 3.2.4) and the R packages survival (version 2.38-3), glmnet (version 2.0-5), clinfun (version 1.0.13), and python (version 3.5.2) were used in the analysis.

Results

Transfer-learning of the CNN model to accurately classify cells in H&E images of HCC

To accurately segment the cell nucleus and recognise the cell type using H&E-stained pathological images of HCC patients, we first adopted a transfer learning procedure (see Materials and Methods) to recognize cancer cells, stromal cells, and lymphocytes in HCC samples (Figure 1), based on a previously developed CNN model for tumour sections of NSCLC [27]. In brief, image patches were randomly selected from whole-slide H&E-stained pathological images of patients with HCC at Beijing Hospital. Each patch was chosen based on the centre surrounding a specific type of cell nuclei, including lymphocytes and tumour and stromal cells. In total, 500 patches for each cell type were selected as training and validation sets for transfer learning, and the cell type in each patch was confirmed by two pathologists (WZ and JZ) from Beijing Hospital (Figure 1).

For the transfer-learning procedure (see Materials and Methods), we adopted a cross-validation method, in which for each round of training and validation, 80% of the image patches were used as the training set, whereas the remaining 20% were used as the validation set. As a result, the overall classification accuracy of the CNN model in the validation set was 96.3% for lymphocytes, 84.7% for stromal cells, and 89.1% for tumour cells, respectively. The independent cross-study classification rates in the test dataset were 93.5% for lymphocytes, 80.3% for stromal cells, and 85.9% for tumour cells.

Spatial features of cells in tumour-section images of HCC patients

We conducted our study with two cohorts of patients: one from Beijing Hospital, which included 67 patients, and the other from TCGA, which included 264 individuals (see Materials and Methods). For each patient, we collected a WSI of the primary tumour. For each WSI, 20 ROIs were selected, with each ROI measuring 5,000 × 5,000 pixels in size (under 400× magnification, see Materials and Methods). For each ROI, we applied our HCC-CNN model to segment and classify each cell nuclei and extracted the x–y coordinates of lymphocytes, tumour cells, and stromal cells. Using these spatial coordinates, we employed Delaunay triangulation [28] as well as the Voronoi diagram [29] to construct topological networks and diagrams of lymphocytes, tumour cells, and stromal cells (supplementary material, Figure S1A–E). Next, we created 109 quantitative image features to characterize the spatial distribution and relationships; a detailed list of these features and their biological implications is provided in supplementary material, Table S1. Examples and a more detailed description of some important spatial features are introduced in Figure 2.

Univariate analysis of spatial features with patient prognosis in the TCGA cohort

With the spatial features obtained for each patient, we explored whether these signatures could help stratify patients into significantly different survival groups.

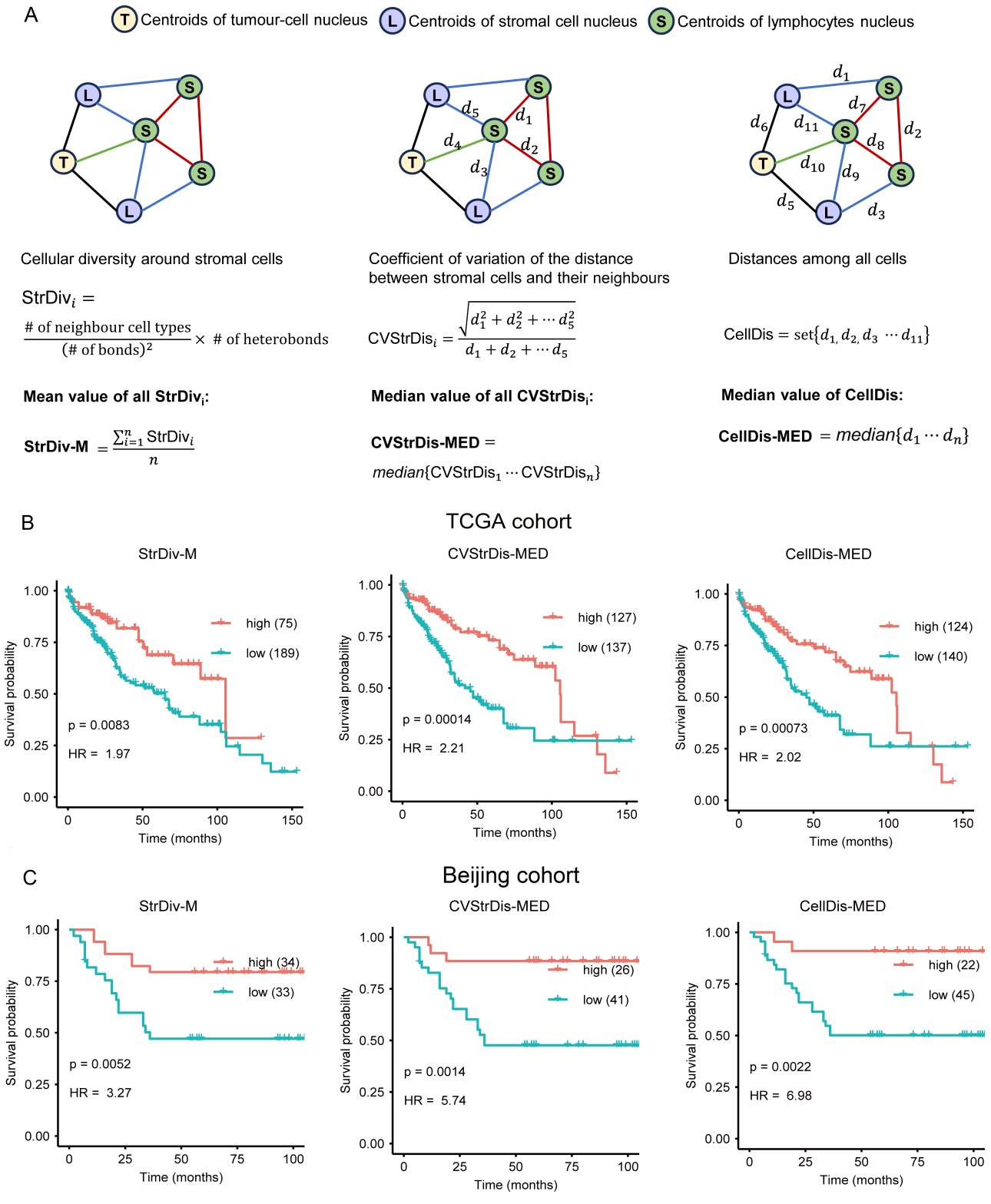

Figure 2. Legend on next page.

We first conducted a univariate analysis of the features using the Cox proportional hazards model (see Materials and Methods). In brief, using the method proposed by package survminerR, we defined the optimal cut-off value of each feature, which allowed us to stratify a patient cohort into two significantly different prognostic groups. The corresponding p values and HRs of the TCGA and Beijing cohorts with the same cut-off are shown in supplementary material, Table S2.

Specifically, we performed such an analysis of the 109 spatial features for the 207 (out of 264) LIHC patients in TCGA (the discovery set) to determine the optimal threshold for each spatial feature. Using the same thresholds discovered, we tested whether they can further stratify both the 57 (out of 264) LIHC patients in TCGA (the validation set) as well as the 67 patients from the Beijing hospital (the independent test set).

To discover the spatial features that can robustly stratify the discovery, validation, and independent test sets, we performed the analysis 10 times and, each time, we randomly selected the 207-patient discovery set from 264 LIHC patients in TCGA. In the end, 6 of 109 spatial features could consistently stratify the discovery (207 patients from TCGA), validation (57 patients from TCGA) and independent test sets (67 patients from Beijing Hospital) into two significantly distinct prognostic groups. Specifically, these 6 features consistently and successfully stratified the 3 sets of patients at least 7 of the 10 times the analysis was performed. The detailed list of the HRs and p values are provided in supplementary material, Table S3.

As examples, Figure 2A illustrates the definitions of three spatial features of the six features identified: the mean value of the cellular diversity around stromal cells (StrDiv-M), the median value of the coefficient of variation of the distance between stromal cells and their neighbours (CVStrDis-MED), and the median distance between cells (CellDis-MED).

In Figure 2B, we demonstrate that, using the same optimal threshold values of corresponding spatial features (StrDiv-M, CVStrDis-MED, CellDis-MED), the three sets of patients can be consistently stratified into better and worse prognostic groups. These results demonstrate that the spatial features derived from this study may robustly capture prognosis-related spatial information inside the WSI across different cohorts. Note that, in this analysis, optimal threshold values of corresponding spatial features were obtained based on the 264 TCGA-LIHC patients.

Moreover, we also tested whether the features correlated with patient prognosis as continuous variables. Specifically, we performed Pearson correlation analysis between the OS of patients from TCGA and Beijing Hospital and the patient-specific values of the six spatial features (see Materials and Methods). All six variables had statistically significant correlation with patient OS for both TCGA and Beijing Hospital cohorts (all $p < 0.05$; supplementary material, Table S4). Especially, StrDiv-M, CVStrDis-MED, and CellDis-MED had correlation coefficients for patients in Beijing Hospital cohorts, with the coefficients all larger than 0.4 (all $p < 0.001$). Thus, these results also suggest that the spatial features developed in this study could be associated with the prognosis of the patient.

On the other hand, we tested the consistency of patient stratification using clinical information, such as age and stage. Note that the cohorts of TCGA and Beijing Hospital had different clinical variables. Only the TNM stage III correlated with patient prognosis for both cohorts (supplementary material, Table S5). Therefore, according to the univariate analysis, the identified spatial features were effective and consistent for patient stratification.

Multivariate analysis of the six spatial features identified

To systematically assess whether the six spatial features identified (Table 1) could serve as independent prognostic factors, we performed multivariate analysis on them with clinical variables, such as sex, age, stage, and treatment information for both TCGA and Beijing Hospital cohorts (supplementary material, Table S6).

Figure 2. Patient stratification efficacy of three important spatial features. (A) Illustration of the spatial features: left – cellular diversity around stromal cells (StrDiv); middle – coefficient of variation of the stromal cell in the Network (CVStrDis); right – the distance between all cells (CellDis). (B) Kaplan–Meier analysis on the overall survival of HCC patients from TCGA (264 patients). Patients were stratified into two groups based on the values of corresponding features. The value-high/low groups are indicated in red and blue, respectively. The optimal cut-off value of each feature was selected for these to reach the lowest log-rank p values (see Materials and Methods). And the corresponding log-rank p values were as indicated. Kaplan–Meier plots for the three spatial features shown in (A), that is, StrDiv-M, CVStrDis-MED, and CellDis-MED, are shown in the left, middle, and right panels, respectively. The specific cut-off values are 0.147, 59.80, and 59.40 for StrDiv-M, CVStrDis-MED, and CellDis-MED, respectively. (C) Kaplan–Meier analysis on the overall survival of HCC patients from Beijing Hospital (67 patients). Patients were stratified into two groups based on the cut-off values defined in (B). Kaplan–Meier plots for the three spatial features shown in (A), that is, StrDiv-M, CVStrDis-MED, and CellDis-MED, are shown in the left, middle, and right panels, respectively.

Table 1. Univariable analyses of factors associated with overall survival on TCGA cohort and Beijing cohort with the same cut-off

	TCGA cohort			Beijing Hospital cohort (with TCGA-derived cut-off values)		
Features	CI	HR	*p*	CI	HR	*p*
StrDiv-M	[1.18, 3.30]	1.97	**0.009**	[1.35, 7.90]	3.27	**0.008**
CVCellDis-MED	[1.39, 3.25]	2.13	**<0.001**	[1.61, 88.60]	11.9	0.015
CVTumDis-M	[1.37, 3.09]	2.06	**0.001**	[1.07, 6.77]	2.69	0.036
CVStrDis-MED	[1.45, 3.35]	2.21	**<0.001**	[1.71, 19.26]	5.74	**0.005**
StrDis-MED	[1.68, 3.93]	2.57	**<0.001**	[1.11, 7.04]	2.79	0.030
CellDis-MED	[1.33, 3.05]	2.02	**0.001**	[1.64, 29.73]	6.98	**0.009**

StrDiv-M: the mean value of all the cellular diversity around stromal cells in the Delaunay network. CVCellDis-MED: the median value of the coefficient of variation of the distance between one cell and neighbours in the Delaunay network. CVTumDis-M: the mean value of the coefficient of variation of the distance between tumour cells and neighbours in the Delaunay network. CVStrDis-MED: the median value of the coefficient of variation of the distance between stromal cells and neighbours in the Delaunay network. StrDis-MED: median distance between stromal cells in the Delaunay network. CellDis-MED: median distance between all cells in the Delaunay network. Significant *p* values are shown in bold font.

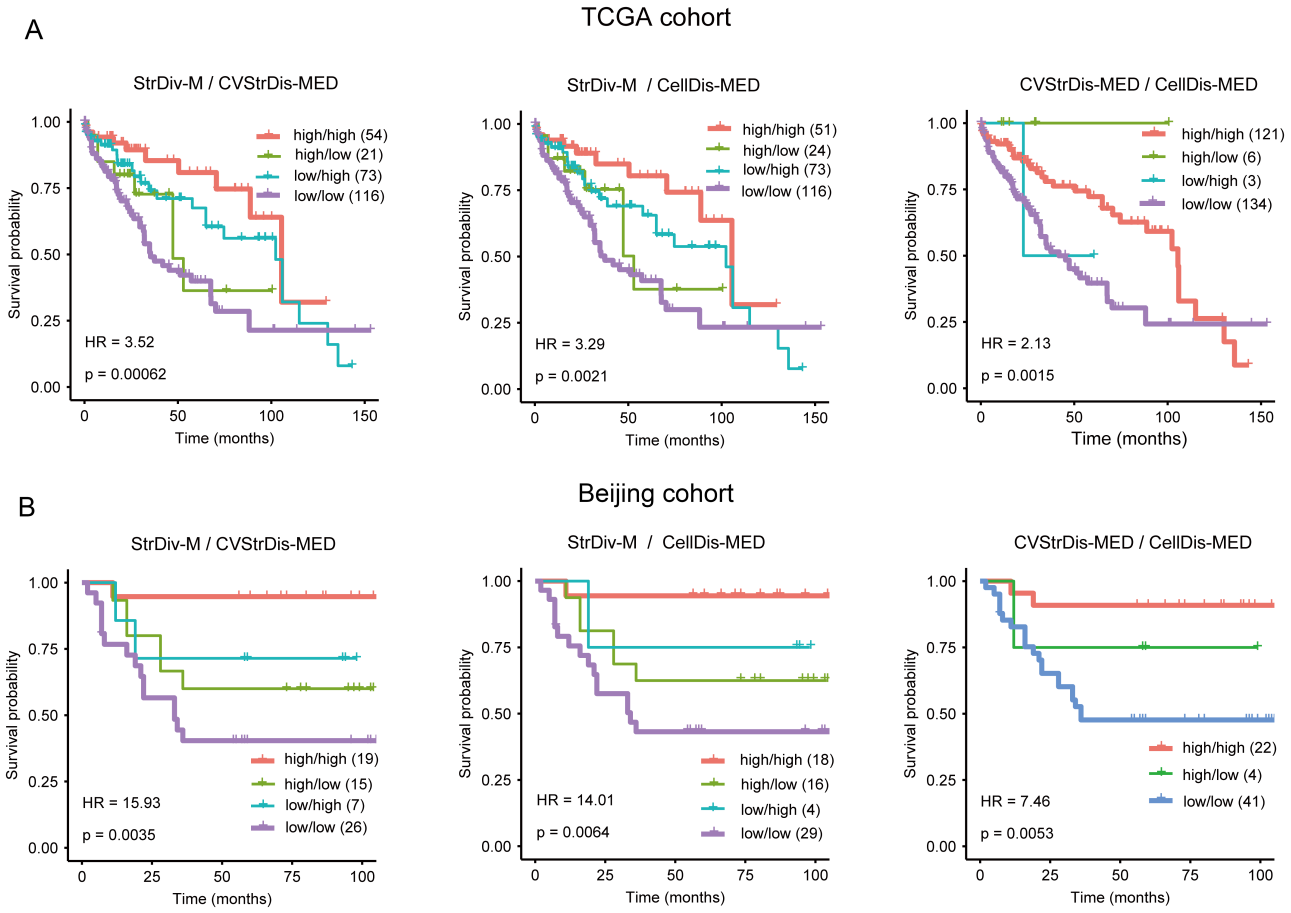

Figure 3. Combinatorial analysis of selected spatial features. StrDiv-MV, CVStrDis-MED, and CellDis-MED were selected for further combinatorial analysis. In (A) and (B), with two of the three spatial features, patients were first separated into two groups based on the cut-off value of one spatial feature. Then the patients can be assigned to one of the four groups based on its value of another spatial feature. Kaplan–Meier analysis was then performed for the four patient groups resulting from the specific combination. The HRs and corresponding log-rank *p* values between the best/worst patient groups were indicated. The results of such combinatorial analysis for TCGA cohort and Beijing hospital cohort using StrDiv-M/CVStrDis-MED, StrDiv-M/CellDis-MED, and CellDis-MED/CVStrDis-MED were given in (A) and (B), respectively.

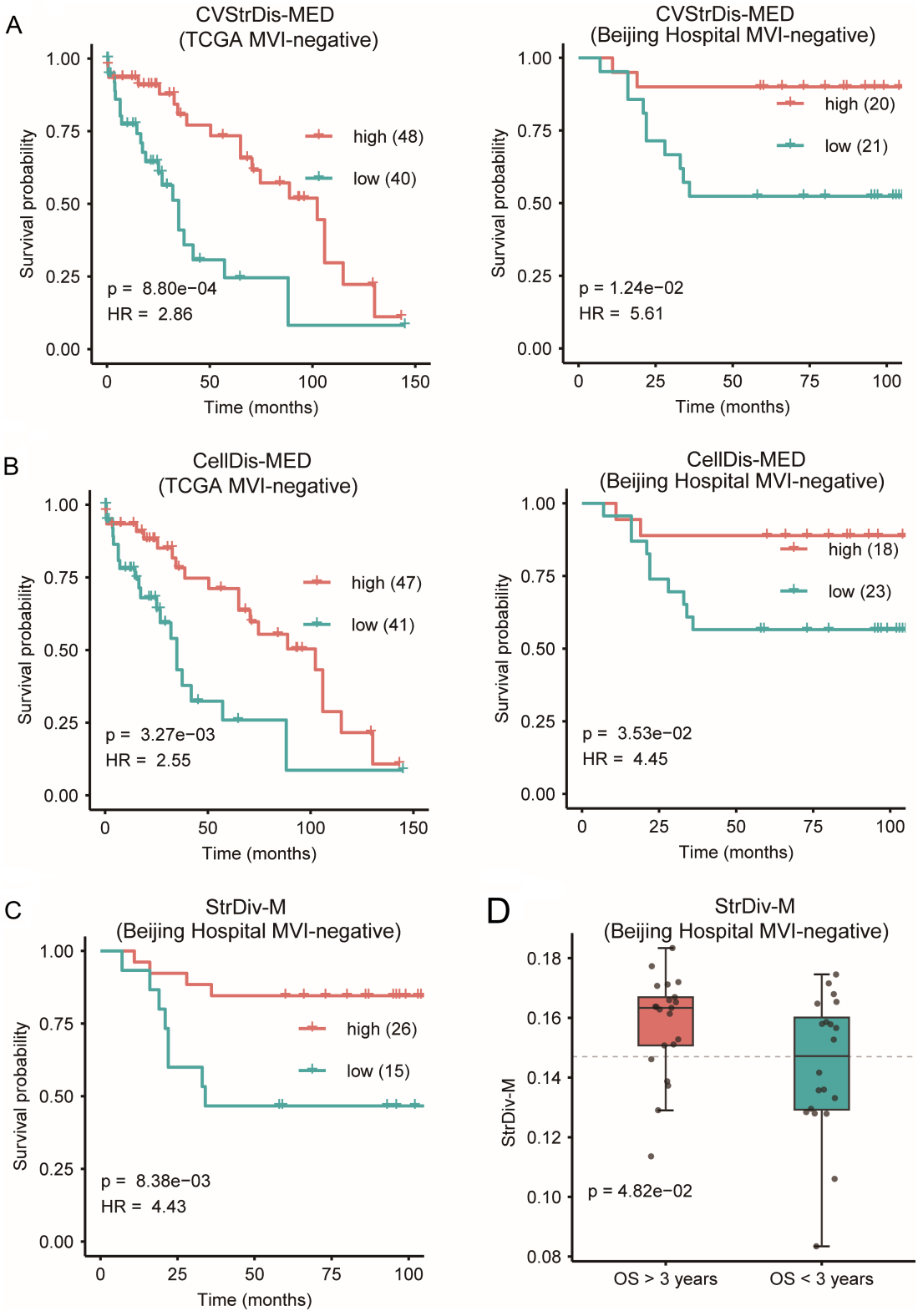

Figure 4. Legend on next page.

Interestingly, our results demonstrated that each of the six spatial features can be independent prognostic factors for both cohorts when they are co-analysed with the clinical features individually.

When we performed multivariate analysis of all six spatial features together with the clinical features, StrDis-MED served as an independent prognostic factor for the TCGA HCC cohort, and StrDiv-M served as an independent prognostic factor for the Beijing Hospital cohort (supplementary material, Table S7).

Furthermore, to systematically test whether combinations of the six spatial features can further stratify the patients, we tried all 15 combinations by selecting two out of six features. We discovered that 14 out of 15 combinations gave general log-rank p values smaller than 0.05 for both TCGA and Beijing Hospital cohorts (supplementary material, Figure S2). Note that each threshold value was the same for the two cohorts. Examples of combinations between StrDiv-M, CellDis-MED, and CVStrDis-MED are shown in Figure 3, all of which have a specific stratification combination with HR >2 and log-rank p values <0.01. These results demonstrate the consistent and significant power of patient stratification for both cohorts using the combination of these spatial features.

Impact of cellular topological characteristics on the prognosis of patients with and without microvascular invasion

To further demonstrate the usefulness of spatial features in patient stratification, we investigated the effects of a combination of spatial characteristics and known clinical diagnostic criteria. Specifically, we chose microvascular invasion (MVI) as an example to explore the potential improvement in patient stratification efficacy.

MVI, which can be classified according to whether MVI occurs [30], has been shown to be an important clinical prognostic index for patients with HCC. However, for both the 264 patients from TCGA cohorts and the 67-patient cohort from the Beijing Hospital, MVI-positive/negative could not significantly separate patients into two prognostic groups (log-rank p value 0.15 and 0.077) (supplementary material, Figure S3). Therefore, we set out to test whether combining the spatial features with the MVI feature could help to improve patient stratification.

Specifically, we discovered that both CVStrDis-MED and CellDis-MED can simultaneously separate the MVI-negative patients into two distinct prognostic groups for both TCGA and Beijing Hospital cohorts (Figure 4A,B). Note that the threshold values for each of the two features were determined by identifying the optimal values in the TCGA cohorts (264 patients) and then applying them to the Beijing Hospital cohorts (67 patients).

For StrDiv-M, interestingly, the optimal threshold derived from the TCGA cohort (264 patients) failed to further stratify the MVI-negative LIHC patients within that group, yet it successfully stratified the MVI-negative patients in the Beijing Hospital cohort (41 patients, Figure 4C). Additionally, we divided the MVI-negative patients into two groups based on OS: those with OS longer than 3 years and those with OS of 3 years or less. As illustrated in Figure 4D, the StrDiv-M values differed significantly between these groups. Notably, these differences were not observed in the TCGA cohort, suggesting the presence of potential Asian-specific cellular spatial features that warrant further investigation in larger cohorts.

As controls, we assessed other clinical parameters between the MVI-positive and MVI-negative groups, but no statistically significant differences were found. Together, these findings indicate that integrating MVI information with the spatial features developed in this study substantially enhances the precision of patient stratification. Future studies should validate the robustness of these results using independent cohorts with well-characterized MVI data.

The correlation between genetic mutations and spatial features

Previous studies have identified the 10 most common and prognostically significant mutated genes in HCC [31]. Building on this work, we analysed the publicly available TCGA-LIHC dataset to examine the relationship between

Figure 4. Efficacy of combinatorial analysis using spatial features and MVI for patients in Beijing Hospital cohort. (A) For MVI-negative patients, the Kaplan–Meier plot demonstrated that patients with low CVStrDis-MED values (blue line) have a significantly longer overall survival for both the TCGA cohort (left) and the Beijing Hospital cohort (right). (B) For MVI-negative patients, the Kaplan–Meier plot demonstrated that patients with low CellDis-MED values (blue line) have a significantly longer overall survival in both the TCGA cohort (left) and the Beijing Hospital cohort (right). (C) For MVI-negative patients, the Kaplan–Meier plot demonstrated that patients with low StrDiv-M values (blue line) have a significantly longer overall survival in the Beijing Hospital cohort. (D) The box plot of StrDiv-M values for MVI-negative patients is shown in the lower panel. Patients with an overall survival shorter and longer than 3 years are shown in blue and red boxes, respectively. The p value of the Student's t test was 0.048.

spatial features and genetic mutations. Our analysis revealed that mutations in the *MEM4*, *RB1*, and *ARID1A* genes were predominantly enriched in the CellDiv-M-high group (CellDiv-M: the mean value of the cellular diversity around all cells), while *FMN2* mutations were significantly enriched in the CvStrDis-MED-high group (supplementary material, Table S8).

Specifically, the CellDiv-M-high group consisted of 32 patients, while the CellDiv-M-low group included 232 patients. Among those in the CellDiv-M-high group, only one patient harboured mutations in *MEM4*, *RB1*, and *ARID1A* (three patients in total), respectively, compared to 25, 25, and 20 patients in the CellDiv-M-low group. Notably, within the CellDiv-M-low group, eight patients exhibited mutations in both *MDM4* and *RB1* genes, one patient had mutations in both *MDM4* and *ARID1A* genes, and another had mutations in both *RB1* and *ARID1A* genes. Additionally, 53 patients carried mutations in only one of the three genes: *MEM4*, *RB1*, or *ARID1A*.

Similarly, the CvStrDis-MED-high group comprised 127 patients, whereas the CvStrDis-MED-low group included 137 patients. Among those in the CvStrDis-MED-high group, 12 patients carried mutations in the *FMN2* gene, in contrast to only one patient in the CvStrDis-MED-low group.

These findings suggest potential connections between the molecular pathogenesis of HCC and the spatial distribution characteristics of the tumour microenvironment.

Discussion

The intrinsic heterogeneity of the TME, both within individual tumours and throughout the spectrum of solid tumours, may contribute to the observed disparities in treatment responses among patients with HCC. The conventional TNM staging system after tumour resection surgery falls short in its predictive capacity for patient prognosis. Consequently, the development of a robust postoperative assessment tool, grounded in the analysis of cellular spatial features using H&E pathological section images of HCC tumours, has significant potential for positively influencing clinical decision making and guiding future therapeutic strategies.

In this study, by employing a transferring learning strategy, we adapted a CNN lung cancer classification model to precisely identify and localize tumour cells, lymphocytes, and stromal cells within H&E pathological section images of HCC patients. Subsequently, we used topological graph analysis to construct novel and quantifiable spatial features of these cells.

Our univariate analysis identified six out of 109 spatial cellular features that consistently and significantly differentiate patient OS across the discovery (TCGA), validation (TCGA), and independent test (Beijing Hospital) sets. Each feature was evaluated using the same cut-off values derived from the discovery set (TCGA). Notably, our multivariate analysis demonstrated that these six spatial features serve as independent prognostic factors when combined with available clinical variables for both TCGA and Beijing Hospital cohorts. Each feature was evaluated using the same cut-off values derived from the TCGA cohort. Furthermore, when integrated with classical clinical features obtained from H&E images, such as MVI status, spatial features like CvStrDis-MED (the median value of the coefficient of variation of the distance between stromal cells and their neighbours) and CellDis-MED (the median distance between cells) consistently enhanced the efficacy of patient stratification across both cohorts.

Although our study has revealed exciting possibilities, including the identification of spatial features as prognostic markers, there are areas where further exploration is warranted, such as further exploration of the interactions between more cell types [32,33], integration of local and global spatial features within the same pathological images [34–36], and the combination of spatial feature analysis with genomic feature analysis [37,38].

In summary, our study, through cell recognition based on a deep-learning approach and the construction of spatial features, developed a novel computational tool that extracts spatial features of the immune microenvironment from H&E pathological images of HCC to assess prognosis. These findings have enhanced our understanding of cell–cell interactions and the spatial heterogeneity of cell distribution within the TME. Ongoing research and the application of spatial morphological distribution analysis hold great promise in deepening our understanding of the complex interactions within the TME, to ultimately contribute to the advancement of personalized medicine and improving the clinical decision-making process.

Acknowledgements

This research was funded by the National Key Research and Development Program of China (2021YFA0911100), National High Level Hospital Clinical Research Funding (BJ-2023-083, BJ-2024-219), the Strategic Priority Research Program of the Chinese Academy of Sciences (XDB0480000), Shenzhen Institute of Synthetic Biology

Scientific Research Program (DWKF20210009), the National Natural Science Foundation of China (32170672, 82073264, and 32000886), the Guangdong Basic and Applied Basic Research Foundation (2021A1515012461), the Shenzhen Science and Technology Program (ZDSYS20220606100606013), and the Guangdong Grants (2021QN02Y554).

Author contributions statement

HH performed the research, including literature search, figure production, study design, data collection/analysis, algorithm development and manuscript writing and editing. TT performed the research, including clinical data collection/analysis and manuscript writing and editing. YL contributed to figure production and data analysis. WL contributed to study design, formal analysis, methodology and manuscript editing. WZ contributed to cell-type annotation, pathological image analysis and algorithm validation and manuscript editing. JZ contributed to cell-type annotation. JC supervised the research, contributed to study design, funding acquisition and manuscript writing and editing. JS supervised the research, contributed to study design, project administration, conceptualisation, funding acquisition and manuscript writing and editing. XL supervised the research, contributed to the study design, project administration, conceptualisation, funding acquisition, literature search, figure production, data analysis/interpretation and manuscript writing and editing.

Data availability statement

Corresponding formalin-fixed paraffin-embedded (FFPE) whole slide images (WSIs) and clinical information of HCC from TCGA were downloaded from https://www.cancer.gov/tcga. The code for constructed features, the training set, and the pre-trained CNN model is available in the open-source domain for research purposes (https://github.com/huhj/Topological-features).

References

1. Njei B. Changing pattern of epidemiology in intrahepatic cholangiocarcinoma. *Hepatology* 2014; **60**: 1107–1108.
2. Choi JH, Thung SN. Advances in histological and molecular classification of hepatocellular carcinoma. *Biomedicine* 2023; **11**: 2582.
3. Mazzaferro V, Regalia E, Doci R, *et al*. Liver transplantation for the treatment of small hepatocellular carcinomas in patients with cirrhosis. *N Engl J Med* 1996; **334**: 693–699.
4. Nomura F, Ohnishi K, Tanabe Y. Clinical features and prognosis of hepatocellular carcinoma with reference to serum alpha-fetoprotein levels. Analysis of 606 patients. *Cancer* 1989; **64**: 1700–1707.
5. Tangkijvanich P, Anukulkarnkusol N, Suwangool P, *et al*. Clinical characteristics and prognosis of hepatocellular carcinoma: analysis based on serum alpha-fetoprotein levels. *J Clin Gastroenterol* 2000; **31**: 302–308.
6. Erstad DJ, Tanabe KK. Prognostic and therapeutic implications of microvascular invasion in hepatocellular carcinoma. *Ann Surg Oncol* 2019; **26**: 1474–1493.
7. Calderaro J, Seraphin TP, Luedde T, *et al*. Artificial intelligence for the prevention and clinical management of hepatocellular carcinoma. *J Hepatol* 2022; **76**: 1348–1361.
8. Larrain C, Torres-Hernandez A, Hewitt DB. Artificial intelligence, machine learning, and deep learning in the diagnosis and management of hepatocellular carcinoma. *Liver* 2024; **4**: 36–50.
9. Ji GW, Zhu FP, Xu Q, *et al*. Machine-learning analysis of contrast-enhanced CT radiomics predicts recurrence of hepatocellular carcinoma after resection: a multi-institutional study. *EBioMedicine* 2019; **50**: 156–165.
10. Peng J, Kang S, Ning Z, *et al*. Residual convolutional neural network for predicting response of transarterial chemoembolization in hepatocellular carcinoma from CT imaging. *Eur Radiol* 2020; **30**: 413–424.
11. Abajian A, Murali N, Savic LJ, *et al*. Predicting treatment response to intra-arterial therapies for hepatocellular carcinoma with the use of supervised machine learning – an artificial intelligence concept. *J Vasc Interv Radiol* 2018; **29**: 850–857.
12. Oezdemir I, Wessner CE, Shaw C, *et al*. Tumor vascular networks depicted in contrast-enhanced ultrasound images as a predictor for transarterial chemoembolization treatment response. *Ultrasound Med Biol* 2020; **46**: 2276–2286.
13. Saillard C, Schmauch B, Laifa O, *et al*. Predicting survival after hepatocellular carcinoma resection using deep learning on histological slides. *Hepatology* 2020; **72**: 2000–2013.
14. Yamashita R, Long J, Saleem A, *et al*. Deep learning predicts postsurgical recurrence of hepatocellular carcinoma from digital histopathologic images. *Sci Rep* 2021; **11**: 2047.
15. Qu WF, Tian MX, Qiu JT, *et al*. Exploring pathological signatures for predicting the recurrence of early-stage hepatocellular carcinoma based on deep learning. *Front Oncol* 2022; **12**: 968202.
16. Zhang S, Yuan L, Danilova L, *et al*. Spatial transcriptomics analysis of neoadjuvant cabozantinib and nivolumab in advanced hepatocellular carcinoma identifies independent mechanisms of resistance and recurrence. *Genome Med* 2023; **15**: 72.
17. Calderaro J, Petitprez F, Becht E, *et al*. Intra-tumoral tertiary lymphoid structures are associated with a low risk of early recurrence of hepatocellular carcinoma. *J Hepatol* 2019; **70**: 58–65.
18. Garnelo M, Tan A, Her Z, *et al*. Interaction between tumour-infiltrating B cells and T cells controls the progression of hepatocellular carcinoma. *Gut* 2017; **66**: 342–351.
19. Wang H, Jiang Y, Li B, *et al*. Single-cell spatial analysis of tumor and immune microenvironment on whole-slide image reveals hepatocellular carcinoma subtypes. *Cancer* 2020; **12**: 3562.
20. Schürch CM, Bhate SS, Barlow GL, *et al*. Coordinated cellular neighborhoods orchestrate antitumoral immunity at the colorectal cancer invasive front. *Cell* 2020; **182**: 1341–1359.e19.

21. Fu T, Dai L, Wu S, *et al*. Spatial architecture of the immune microenvironment orchestrates tumor immunity and therapeutic response. *J Hematol Oncol* 2021; **14**: 98.
22. Karimi E, Yu MW, Maritan SM, *et al*. Single-cell spatial immune landscapes of primary and metastatic brain tumours. *Nature* 2023; **614**: 555–563.
23. Sorin M, Rezanejad M, Karimi E, *et al*. Single-cell spatial landscapes of the lung tumour immune microenvironment. *Nature* 2023; **614**: 548–554.
24. Ruifrok AC, Johnston DA. Quantification of histochemical staining by color deconvolution. *Anal Quant Cytol Histol* 2001; **23**: 291–299.
25. Ciecholewski M. River channel segmentation in polarimetric sar images: watershed transform combined with average contrast maximisation. *Expert Syst Appl* 2017; **82**: 196–215.
26. Li X, Zhang R, Wang Y, *et al*. Automatic segmentation of hepatocellular nuclei in fluorescence microscopy images based on graph cut and closed polygonal line. *Sci Rep* 2020; **10**: 13342.
27. Wang S, Wang T, Yang L, *et al*. Convpath: a software tool for lung adenocarcinoma digital pathological image analysis aided by a convolutional neural network. *EBioMedicine* 2019; **50**: 103–110.
28. Delaunay B. Sur les polygones et les polyèdres. *Bull Acad Sci USSR* 2007; **6**: 793–800.
29. Bern NA. Surface reconstruction by voronoi filtering. *Discrete Comput Geom* 1999; **22**: 481–504.
30. Shi JY, Wang X, Ding GY, *et al*. Exploring prognostic indicators in the pathological images of hepatocellular carcinoma based on deep learning. *Gut* 2021; **70**: 951–961.
31. Chen M, Zhang B, Topatana W, *et al*. Classification and mutation prediction based on histopathology H&E images in liver cancer using deep learning. *npj Precis Onc* 2020; **4**: 14.
32. Wang P-C, Hu Z-Q, Zhou S-L, *et al*. The spatial distribution of immune cell subpopulations in hepatocellular carcinoma. *Cancer Sci* 2022; **113**: 423–431.
33. Rong R, Sheng H, Jin KW, *et al*. A deep learning approach for histology-based nucleus segmentation and tumor microenvironment characterization. *Mod Pathol* 2023; **36**: 100196.
34. Ahmedt-Aristizabal D, Armin MA, Denman S, *et al*. A survey on graph-based deep learning for computational histopathology. *Comput Med Imaging Graph* 2022; **95**: 102027.
35. Bera K, Schalper KA, Rimm DL, *et al*. Artificial intelligence in digital pathology – new tools for diagnosis and precision oncology. *Nat Rev Clin Oncol* 2019; **16**: 703–715.
36. Gurcan MN, Boucheron LE, Can A, *et al*. Histopathological image analysis: a review. *IEEE Rev Biomed Eng* 2009; **2**: 147–171.
37. Chen M, Zhang B, Topatana W, *et al*. Classification and mutation prediction based on histopathology H&E images in liver cancer using deep learning. *NPJ Precis Oncol* 2020; **4**: 14.
38. Zeng Q, Klein C, Caruso S, *et al*. Artificial intelligence-based pathology as a biomarker of sensitivity to atezolizumab-bevacizumab in patients with hepatocellular carcinoma: a multicentre retrospective study. *Lancet Oncol* 2023; **24**: 1411–1422.

SUPPLEMENTARY MATERIAL ONLINE

Figure S1. The workflow to construct space features.

Figure S2. The combination of all six factors can further help to identify the worst and best prognostic groups.

Figure S3. MVI status does not significantly separate patients into two prognostic groups.

Table S1. Full list of spatial features and their biological implications.

Table S2. Detailed list of the hazard ratios and log rank *p* values of all the constructed features.

Table S3. Ten-fold cross-validation analysis on the discovery, validation, and independent test sets.

Table S4. Pearson correlation analysis between patient overall survival (OS) and the values of six spatial features.

Table S5. The consistency of patient stratification using clinical information.

Table S6. Multivariate Cox analysis of each selected spatial and clinical feature with overall survival on the TCGA and Beijing cohorts.

Table S7. Multivariate analysis of all six spatial features with the clinical features.

Table S8. Analysis of the publicly available TCGA-LIHC dataset to examine the relationship between spatial features and genetic mutations.